

Version: March 15, 1996

**The Spatial Intensity Distribution of the UV light in HH objects.
Revisited.**

Amaya Moro Martin

Maria Mitchell observatory, Nantucket, MA 02554

email: mamoro@mimo.org

Alberto Noriega-Crespo

Infrared Processing and Analysis Center, CalTech-JPL, Pasadena, CA 91125

and Maria Mitchell Observatory, Nantucket, M A 02554

email: alberto@ipac.caltech.edu

Karl-Heinz Böhm

Department of Astronomy FM-20, University of Washington, Seattle, WA 98195

email: bohm@astro.washington.edu

and

Alejandro C. Raga

Instituto de Astronomía, UNAM, 04510, México D.F., México

email: raga@astrocu.unam.mx

RESUMEN

Muchas de las características observadas en objetos Herbig-Haro han podido ser reproducidas mediante modelos de choque. Se muestra que modelos similares pueden aplicarse para la distribución espacial de intensidad de las líneas ultravioleta observadas por IUE. Se han utilizado espectros del archivo de IUE para estudiar las líneas ultravioleta (C IV $\lambda 1549$,

Si III] $\lambda 1891$, C I I I] $\lambda 1909$, C II] $\lambda 2326$, Mg II $\lambda 2799$) y también el continuo (modelado como continuo de dos fotones), de 10S objetos: 1111 1, 1111 2(H+ A⁺), III 2(G+B), III 24A, 1111 32A, 1111 43(A+B+C) y 1111 47A. Los datos de IUE tienen una calidad limitada, debido a lo amplio de su función de ensanchamiento de punto y su baja señal a ruido, y por tanto han sido degradados para compararlos con las observaciones. Los parámetros físicos de los modelos se basan en estudios ópticos anteriores y fueron variados dentro de sus intervalos de incertidumbre para reproducir las observaciones. Los objetos se modelaron como un único choque de protones (i.e. 11111, 1111 24A, 1111 32A & III 47A) o la superposición de dos (i.e. III 2(11-1A⁺) & 1111 2(G+B)) o más (i.e. III 43(A+B+C)). La idea es tomar en cuenta la compleja estructura de estos objetos y la contribución de otras condensaciones a la luz ultravioleta dentro del abertura de IUE. Los modelos dan una descripción razonable de las distribuciones espaciales de intensidad de los objetos 1111 obtenidas por IUE, y un método para entender observaciones futuras de mayor resolución espacial.

Received _____, accepted ----- .. -----.

ABSTRACT

Simple kinematical bow shock models have successfully explained many of the observed features in Herbig-Haro objects. It is shown that similar models can be applied to the spatial intensity distribution of the UV lines observed by IUE. Archival IUE spectra have been used for the objects 11111, III 2(II-} A⁺), 1111 2(G+B), III 24A, 1111 32A, III 43(A-} B+C) and III 47A, where the brightest UV lines (C IV λ 1549, Si III] λ 1891, C III] λ 1909, C III] λ 2326, Mg II λ 2799) were studied, as well as the UV continuum (modeled by a two photon continuum). The quality of the IUE data is rather limited due to the broad point spread function and the low signal-to-noise ratio, and therefore the models were degraded to make them comparable to the observations. The physical parameters used in the models were obtained from previous optical studies and varied accordingly to match the observations, but within the known uncertainties. The objects were modeled by a single (i.e. III 1, III 24A, III 32A & III 47A) or the superposition of two (i.e. 1111 2(II+A⁺) & 1111 2(G+B) or more (i.e. III 43(A-} B+C)) bow shock models. The idea was to take into account the complexity of the morphology of these objects, and the contribution to the UV light from different condensations within the IUE aperture. The models provide a reasonable description of the available IUE observations of 1111 objects spatial intensity distribution, and a method to understand future UV higher spatial resolution observations.

1. Introduction

Herbig-Haro (HH) objects are diffuse emitting regions associated with the supersonic outflow from young stellar objects (YSOs). A large fraction of their UV, optical and near infrared emission is in the form of permitted (e.g. $H\alpha$, C IV) and forbidden (e.g. [S II], [Fe II]) lines, which arise in the recombination region of the shock excited gas (Schwartz 1975), a consequence of their supersonic interaction with the surrounding medium. The HH condensations in many cases resemble morphologically working surfaces, which are characterized by two shocks, the Mach disk (or jet shock) and the bow shock (e.g. Hartigan 1989; Raga 1989). In detail, however, their structure is more complex, as ground (Eislöffel et al. 1994) and HST images (Hester et al. 1994) have recently revealed.

Several of the intrinsic properties of such HH objects, e.g. intensity line ratios, position-velocity diagrams, velocity dispersion and their optical *spatial intensity distribution* (hereafter SID), have been modelled in a reasonable way by simple kinematical bow shock models. The success on these models relies on the difficulty in spatially resolving for most targets the Mach and bow shocks; that the bow shock allows the simultaneous presence of strong shocks at its apex, and weaker shock at its wings; and finally, that for the typical estimated jet and preshock densities (Raga & Noriega-Crespo 1993) the bow shock dominates the optical emission (e.g. Hartigan 1989; Raga 1989).

In the UV HH objects display a wide range of emission line excitations, from C IV $\lambda 1550$ to Mg II $\lambda 2799$, which can be easily explained in the context of a bow shock structure. In a curved shock it is only the perpendicular component of the shock velocity which becomes thermalized, this makes possible to have high excitation lines near the apex, and low excitation ones arising from the wings of a bow shock (see e.g. Böhm 1989; Brugel 1989).

The goal of this paper is to compare the IUE SID of the UV light observed in HH objects, with those predicted by kinematical bow shock models. Although a comparison between the

1 UE data and ‘degraded’ optical observations has been previously carried out by Lee et al. (1988), the comparison with the shock models should provide a more clear understanding of the physical conditions in 1111 objects. The IUE data has been collected from the published literature (Lee et al. 1988; Böhm et al. 1987; Böhm et al. 1991; Böhm et al. 1992; Böhm et al. 1993). The objects studied are III 1, III 2, 1111 24A, III 32, 1111 43, and III 47, with a particular attention to their stronger emission lines: C IV λ 1549, C III] λ 1909, C II] λ 2326, Mg II λ 2799, Si III] λ 1891 (if available) and the continuum.

A description of the properties and limitations of the kinematical bow shock model is presented in §1, and of the shock models for the selected lines in §3. The characteristics of the individual 1111 objects are discussed in §4, and we present our concluding remarks in §5.

It is shown, as suspected from the optical observations (Eislöffel et al. 1994; Hester et al. 1994) and model position-velocity diagrams (Indebetouw & Noriega-Crespo, 1995) that the match between theory and observations improves when the presence of multiple condensations is considered in their interpretation.

2. The Kinematical Bow Shock Model

2.1. Geometry

A detailed description of a simplified bow shock model can be found for instance in Hartigan, Raymond & Hartmann 1987 (hereafter HH87). The basic idea is the following. In the frame of reference of the shock, the preshocked gas enters the bow shock at a velocity V_S , and angle ξ (see Figure 1). To simplify the calculations of the line emission, the bow shock is divided into a number of annuli of constant ξ . Once the shape of the bow shock is known (at an orientation ϕ), ξ and therefore the perpendicular component of the velocity, V_\perp , can be determined. Since it is only this component which transforms its kinetic energy into internal

energy, the emission from each annulus is calculated running a plane-parallel shock model with velocity equal to its corresponding V_{\perp} . This emission, which is considered to be generated in an infinitesimal shell, is then weighted by the area of the annulus and co-added with the emission coming from the rest of the annuli, giving the line emission over the entire bow shock. For a given line the S11) is obtained by integrating the emission along the bow shock symmetry axis. The final distribution is convolved with a Gaussian with a width given by the point-spread function (PSF) of the instrument. The IUE PSF is between 4" and 5", depending on the wavelength (see e.g. de Boer & Meade 1981). The models are then normalized to the size of the object (R_0), so that the resulting distributions are scale-free, and to the peak intensity value (I_0).

The planar shock models come from H1187, and have been carefully interpolated to be mapped smoothly onto the bow shock model (see Figure 2, bottom panel). A good interpolation is specially necessary for the low velocity shocks, given their important contribution to the intensity over the large surface area of the bow shock wings. An example of this can be seen in the intensity distribution of Mg II $\lambda 2799$, where both interpolation and grid resolution 'conspire' as to generate some noise at the wings (see Figure 2). In most cases the grid size of $N=500$ elements was enough to minimize the noise.

2.2. The grid of models

The input parameters of the models are set by the available plane parallel shock models from H1187, the UV emission lines observed by IUE, and the geometry of our kinematical bow shock. The lines studied are N V $\lambda 1240$, C II $\lambda 1336$, N IV] $\lambda 1486$, C IV $\lambda 1549$, O III] $\lambda 1663$, Si III] $\lambda 1891$, C III] $\lambda 2326$, Mg II $\lambda 2799$ and the two-photon continuum. For the shocks the following parameters were considered: (1) the shock velocity (100, 150, 200, 250 km S⁻¹), (2) the angle between the bow shock axis and the plane of the sky (0°, 300°), (3) the preshock

density ($100, 1000 \text{ cm}^{-3}$), and (4) the preshock ionization state of the gas. For this last one fully ionized or local equilibrium were the choices (see HRII87), although it is known that the preionization structure in a bow shock is more complex, and that in many comparisons equilibrium models seem to match better the observations (Noriega-Crespo et al. 1989). In all cases, given the wide aperture of IUE, the models considered a slit 10 times the size of the obstacle and at a fix 0° orientation with respect the bow shock axis.

As examples of the S11) directly obtained from the bow shock models, i.e. without convolving with the IUE PSF, the models for the lines C IV and Mg II are presented in Figure 2 (equilibrium and fully ionization for $n = 100 \text{ cm}^{-3}$ and $\phi = 0^\circ$). These two lines were chosen because they show the overall behavior that is seen in the high and low excitation lines.

Some general features that can be identified from the grid of models are the following: (1) The emitting region gets wider as the shock velocity increases. In fact the full width at 0 intensity (FWZI) for a low excitation line is approximately equal to the shock velocity (HRII87). (2) The preionization state affects the spatial distribution of the emission lines. A fully ionized medium gives different and wider looking distribution than the equilibrium one, since for the same shock velocity its energy does not go into ionizing the preshock gas. For our bow shock model it means that weaker shocks along the wings can still released some of their energy in emission. (3) As the angle between the axis and the plane of the sky (ϕ) increases the profiles become smoother, which it is expected from the geometry of the bow shock. (4) Some structure seen at a few radii from the stagnation region in the distributions is due to a combination of the 'coarseness' of the geometrical grid with the finite interpolation of the plane parallel models.

The relationship between intensity versus shock velocity is also shown in Figure 2 for the corresponding lines. Notice that difference between the spatial distributions can be traced back to those already present in the shock models of each line. For example the small 'bumps'

in the fully preionized shock models for the Mg II $\lambda 2800$ line, become amplified by the extent emitting area of the bow shock wings.

2.3. Limitations of the model

Some important limitations of the bow shock model described above are the following:

- (1) The preshock ionization state is not well known: the preshock material entering a certain annulus is not only being ionized by the photons coming from this annulus but also by the ones next to it. Improved bow shock models have been developed (Raymond et al. 1988) and seem to agree slightly better with the observations.
- (2) Planar shock models are not reliable in the low velocity range. This fact, together with the projection problems arising when using high orientation angles (ϕ) and integration intervals larger than $7 R_0$, make it difficult to model low excitation 1111 objects, as 111143, where the shock velocities are relatively low.
- (3) Knowledge about the preshock magnetic field and the radiative transfer parameter is very limited, parameters that become important in the low velocity shocks.
- (4) The model assumes a medium with a uniform density, which could not be the case. Preshock density is not well known.
- (5) 1111 objects present more complex structures than the single, double and triple condensation models studied in this paper.
- (6) The model does not take into account emission from the Mack disk and working surface of the jet itself. Thermal instabilities are neglected, as well as molecular cooling.

3. General Remarks and Results

3.1. IUE data

The observations used in this project were obtained by IUE (see table 1 for details). It has been pointed out several times the limitations of IUE for the study of III objects (see

e.g. review by Böhm 1990), nevertheless is one of the few instruments that have provided us with simultaneous information of the spatial and spectral properties of these objects at ultraviolet wavelengths. The main caveats to study the 1111 objects SII in the UV are due to their relatively low surface brightness, the fact that they are found in star forming regions which are not necessarily transparent to the UV light, plus the limited spatial resolution given the broad PSF of the IUE telescope.

To deal with these problems, we have concentrated on the shape of the *normalized* intensity distribution for a given line, avoiding reddening corrections. We have performed also a convolution of the models with the IUE PSF to avoid deconvolving the observations, which it is proven to be more difficult and less reliable (see e.g. Lee et al 1988). The IUE PSF varies as a function of wavelength, and so it was taken as a Gaussian with a FWHM of $4''$, for the C IV and Mg II lines and $5''$ for C II], C III], Si III] and the continuum (de Boer & Meade, 1981). Since the size for many of these objects, from the ground at optical wavelengths, are $\sim 5''$ most of the spatial details are lost in the convolution. If the size of the UV emitting region, however, is *larger* than $5''$, then it becomes very interesting the comparison with the models as well as their interpretation (see below).

In the present models the angle between the slit and the symmetry axis has been taken to be zero, since the projected size of the slit on the plane of the sky ($23''$) is larger than the object ($\sim 5 - 7''$ in size in general). The sensitivity of the instrument changes along the aperture, reaching a maximum at the center and declining steeply towards the extremes (Clarke & Moos, 1981). This fact, together with the increasing faintness of the III] object further along the wings, makes it very difficult to get reliable information near the extremes of the slit.

The models have been shifted to match the peak intensity distribution of the most reliable observed line. Once this is done the relative shift for all the other comparison lines, for the

same exposure, is identical. We selected C IV $\lambda 1549$ for the short and C II $\lambda 2326$ for the long wavelength ranges to match the maxima.

Since 1111 objects are not point sources, but diffuse emitting regions with a given morphology, it is necessary to know the orientation of the slit with respect to the object, which depends on the spacecraft roll angle and the orientation of the object in the sky. This information now is easily available from the IUE data base home page (<http://banzao.gsfc.nasa.gov/IUE/search>). optical images in [S II] and H-alpha were used to determine the position angle of the objects (see section 3.2 for references). The order numbers in the spectra increases in the direction from the large aperture toward the small aperture for the SWP and LWR cameras, and it goes in the opposite way for the LW camera (Turnrose et al. 1984).

Finally bear in mind that when comparing models with the IUE observations of 1111 objects, most of the published data *do not* show error bars. For the brightest objects like III 1 and III 2 a typical estimate of the uncertainties in the fluxes is $\sim 10\%-15\%$. For fainter objects like III 43, III 47 and specially III 24 the uncertainties can be a lot larger.

3.2. The Spatial Intensity Distributions

The physical parameters for the models were obtained from ground base optical studies (a list of them is shown in table 2). The initial parameter space was based on the best available shock velocities, proper motions, radial velocities and optical spectra. In some cases the input numbers for the models were varied within the known uncertainties, although, as previously pointed out, it is difficult to try to constrain theoretical models completely using IUE observations.

The models depend on two angles. One from the relative orientation of the object in the

sky with respect to the observer, and the angle between the symmetry axis of the object and the position of the slit. In practice we found that this second angle did not make a significant difference for most models, given the large aperture of the 1 M line-by-line observations ($\sim 10'' \times 23''$) in relationship to the size of the 1111 objects. In the models we assume that the slit aperture encloses completely the object.

The superposition of multiple bow shock models was carried out in the following way. A model for an individual condensations was generated, and then size and flux were scaled accordingly (by the same factor) to one of the observed condensations (the brightest one). Next, bow shock models for the other individual condensations were calculated and shifted with respect to the one taken as a reference by their corresponding amount (obtained from the optical images), and then were added.

The models which resemble more the observations were those calculated under the assumption of equilibrium preionization. Fully preionized and equilibrium plane shock models are identical for shock velocities above 180 km s^{-1} (111/1187). The difference arises at low velocities, which manifest themselves along the bow shock wings. Because of this, the low velocity shocks control the extent and shape of the 'tails' in the S11)s, particularly for the low excitation lines. So with the exception of III 32A (see Table 2) the peak velocity of the III objects considered lies below the 180 km s^{-1} threshold, and therefore, both equilibrium and fully ionized models were calculated. The later ones, however, do not match as well the observations, except perhaps for 1111 32A (see below). A similar conclusion was reached by Noriega-Crespo et al. (1989) with respect to the optical forbidden lines.

The main focus of this study is the shape of the S11)s, although for consistency the integrated fluxes of the models and the observations were also compared. The fluxes match within factors of 2 and 10, except for the two photon continuum where the factors are higher, a direct consequence from the fact that the plane parallel shock models overestimated the two

photon continuum flux (IRI87). The observations have been gathered from those published by Lee et al. (1988), Böhm et al. (1987), and Böhm et al. (1993).

4. Discussion on Individual Objects

4.1. III 1

III 1 is a high-excitation object and one of the brightest in the ultraviolet (together with III 2). We have modeled it as a single condensation with a shock velocity of 175 km s^{-1} , an orientation angle $\phi = 5^\circ$ (moving into the plane of the sky), a preshock density of 100 cm^{-3} , and a radius $R_0 = 2''$. Figure 3 shows a comparison between the IUE observations and the models for 2 selected emission lines: C IV $\lambda 1550$ and Si III $\lambda 1891$, and two 200 \AA wide continuum bands, $1500\text{-}1700 \text{ \AA}$ & $1700\text{-}1900 \text{ \AA}$. These models assume equilibrium pre-ionization. In Figure 3 (and all the rest) the broken line represents the IUE PSF and the solid line the convolution of the model with the PSF.

It is interesting to notice that the IUE observations are in this case wider than the PSF, which suggests that the condensation was resolved (but see below). The single condensation models are just slightly wider than the PSF, but not as much as the observations. This would seem to indicate that the UV emission is not limited to only the stagnation zone where the shock is completely thermalized, but it is more extended. This is a bit surprising for the C IV and Si III lines, since it is expected that their emission arises from the 'apex' where enough energy is available for their excitation, after the thermalization of relatively fast shock waves. The observed shapes of the SIDs are themselves quite different from a Gaussian PSF, something which becomes more evident when looking at the continuum emission. Only in the case of the C IV $\lambda 1549$ from the SWP24914 exposure, the observed distribution has a comparable extent as the model. Notice that the corresponding SID from the SWP40657

exposure, which was taken at a similar orientation and roll angles, it does look broader.

The comparison between model and observation]! leads to at least two things, one that the preionization is not entirely near equilibrium. The full preionized models, although do not look like the observations and overestimate the integrated fluxes, have in general S11) with a more extended shape. An intermediate preionization state seems likely. Second, that some of high excitation UV emission could arise from smaller condensations which are not resolved; a strong possibility by judging the complex morphology of the high spatial resolution 11 ST observations.

4.2. III 2 (H+A ') and III 2 (G+B)

The 11 II 2 object, which is the southern bipolar counterpart of 11111, has a high excitation and a very complex structure (see e.g. Eislöffel et al. 1994; Schwartz et al. 1993, Hester et al. 1994). We modeled 1111 2 (H+A ') as the superposition of two bow shock models with a preshock density of 100 cm^{-3} and equilibrium pre-ionization. The shock velocity and orientation angles used to model III 2H and III 2A ' were 125 km s^{-1} and 2° , and 170 km s^{-1} and 12° respectively (following Indebetouw & Noriega-Crespo 1995), with both objects moving into the plane of the sky.

Since from ground base observations III 2H alone displays an almost elliptical shape, we considered in the models a minimum and maximum value for its size depending on the location of the 1 UF aperture (see Table 2). Recall that the models assume an spherical obstacle for the formation of the bow shock. The separation between III 2H and III 2A ' changes a bit accordingly and was also included in the models. In practice, these are minor adjustments to the resulting S11)s, since it is the superposition of two bow shocks what determines mostly the S11) shape. The radii for III 2H, III 2A ' and their separation were determined from the FWHM of images taken by 2 meter-like telescopes in [S II] and H α (Lee et al. 1988, Böhm et

al. 1991, 1991 et al. 1990).

Observationally (see Figures 4a, b), the distributions for the C IV and C III] lines in the SWP18157 and SWP40663 frames are wider than the point spread function (broken line). This was the first indication of contribution of more than one condensation to the UV light. The superimposed double bow shock model does a very good job in matching the extent of the SWP40663 lines (Figure 4a). The 'hump' of the model distribution suggests that the double peak structure that is observed is for real and not an artifact of the IUE observations. At a different orientation for the SWP18157 frame, the superimposed model resembles that observations both in shape and extent.

There is another condensation that has been observed in III 2: III 2G. The optics] images suggest that III 2G emission may have a contribution from III 2B within the IUE aperture, so once again we tried the superposition of two bow shocks to model its overall UV emission. III 2B is a small condensation and its size was determined using some 3.5 III 2 sub-arcsecond images (Reipurth et al. 1993). Recall that the models use the radius of the object, but in practice what is measured is the FWHM size of a condensation and this is taken as its diameter. The values quoted in Table 2 correspond to half this value.

The models that better match the observations assume a radius $R_0 = 0.9''$ for III 2G and $0.4''$ for III 2B, and a distance between condensations of $2.8''$ (see Figure 4c). Equilibrium preionization and a 100 cm^{-3} preshock density were used. The shock velocities and the angles between the axis and the plane of the sky were derived from the proper motions (Eislöffe et al. 1994) and the radial velocities (Böhm et al. 1992). Although both objects are essentially in the plane of the sky, we use -5° for III 2G (moving towards the observer) and 2° for III 2B (moving into the sky). In practice the distributions do not depend on these values. The IIS'1' images tentatively indicate the presence of [O III] in III 2G (Hester et al. 1994), which suggests shock velocities of $\sim 100 \text{ km s}^{-1}$. In the models, therefore, velocities of this

order were considered. The models in Figure 4c correspond to 110 km S-1 for HII 2G and 105 km S-1 for HII 2B. The observed distributions for C IV and C III] from the SWP43891 set (Böhm et al. 1993) are again broader than the PSF. The superimposed double bow shock model does match well the extent of the C III] line and it is somewhat narrower than the observed C IV distribution. One suspects that a more realistic preionization in the models could give even a better match.

4.3. HII 24A

HII 24 is optically a remarkable object with a very complex morphology, and situated among two or three outflows (see e.g. Mundt, Ray & Raga 1991). One of the bright condensations corresponds to HII 24A which was observed in the UV by Böhm et al. (1992). HII 24A although optically seems to be a high excitation object (see e.g. Brugel et al. 1981) in the UV does not belong neither to the high nor to the low excitation categories (Böhm et al. 1992). The lack of UV emission lines has lead to the analysis of just its continuum emission, which it has a SID wider than that in the [S II] 6717/31 optical lines (Böhm et al. 1992), for instance.

Despite the complexity of HII 24, the extended nature of condensation A, and our temptation to use a superposition of two bow shock models to explain the observed wide SID, the nearest bright condensation HII 24E is $\sim 20''$ apart, and therefore we decide to model it as a single bow shock. We considered two shock velocity models for it. On one hand the proper motions (Jones et al. 1987) and the velocity dispersion of its optical lines, e.g. H α , [N II] $\lambda 6583$ and [S II] $\lambda 6731$ (Solf 1987), suggests a shock velocity relatively low ~ 50 km S-1. On the other hand the detection of [O III] $\lambda 5007$ (Brugel et al. 1991) implies a shock velocity of ~ 100 km s $^{-1}$. Both bow shock models (for 50 and 100 km s $^{-1}$) assume equilibrium preionization with a preshock density of 100 cm $^{-3}$, a radius of 3 " and an angle of $\sim 36^\circ$ (towards

the observer).

In Figure 5 we show the comparison with the observations of two different 200 \AA wide continuum bands, $1300 - 1500$ and $1600 - 1800$. The top two panels correspond to the 50 km s^{-1} model and the bottom one to the 100 km s^{-1} model. The comparison with the SWP22708, at an orientation of 153° , with the 50 km s^{-1} bow shock model looks very good, both observation and model are hardly wider than the PSF. In the next two panels we consider the SWP38033 and SWP38102 observations, taken at slightly different aperture orientation angles $\sim 13^\circ$ apart, but more than 150° with respect the SWP22708 (see Table 1). The observed SIDs are considerable wider than the calculated at 50 km s^{-1} (middle panel), as was the case with the optical lines (Böhm et al. 1992). The 100 km s^{-1} model (bottom panel) looks better thanks to the tail generated by the low velocity shocks, but still it is not as wide as the observations.

We don't have a simple explanation for these differences, although we suspect, given the relative faintness of III 24, that some of the broadening of the observed S11) could be due to differences in the zero intensity level during the data reduction, since there is a tendency to overestimate the measured flux in low signal-to-noise spectra.

4.4. 111? 32A

From the ground base observations III 32 can be characterized by three bright condensations (see e.g. Hartigan, Mundt & Stocke 1986; Davis, Eislöffel & Smith 1996). Condensation A is optically the brightest with a complex morphology and the one studied by IUE. 1111 32A displays a high excitation (see e.g. Hartigan et al. 1986), with a strong $[O III] \lambda 5007$ emission, and also a high extinction, with an $E(B-V) \sim 0.6$ (see e.g. Brugel et al. 1981).

The only IUE data available is that for the $Mg II \lambda 2800$ line, due to the strong effect

Of the extinction at smaller wavelengths (Lee et al. 1993). We consider bow shock models at two different orientation angles in the plane of the sky, 30° (Davis et al. 1996) and 70° (Self, Böhm & Raga 1986). Based on the mentioned spectroscopic data and radial velocity measurements, plus III 32A proper motions (Herbig & Jones 1983) we selected a shock velocity of 300 km s^{-1} . A preshock density of 100 cm^{-3} and a radius of $R_0 = 2.5''$ were used. Models at both preionizations were calculated, but in this case the completely ionized models, show in Figure 6, resemble more the observed SIDs. The LWR13004 observations are wider than the PSF (broken line) and with a tail; a trend reproduced by the models at 30° (top) and 70° (bottom).

4.5. 1111 43 and III 47A

Both 1111 43 and III 47A are low excitation objects, with spectral features from fluorescent H_2 emission and UV continuum (Böhm et al. 1991). Because of the lack of available one-dimensional H_2 emission shock models from HRL87, we have focused on the distribution continuum emission from both objects. In Figures 7 & 8 we show the SIDs for III 43 and 1111 47A, respectively, for the SWP24924, LWP4041, SWP31828 and SWP33960 observations.

The III 43 system was modeled as a triple condensation (A+B+C) with a preshock density of 100 cm^{-3} and equilibrium preionization for each condensation. From the analysis of the data presented by Schwartz (1988), III 43A was modeled with a shock velocity of 100 km s^{-1} at an orientation angle of 60° into the sky. For III 43B the shock velocity was chosen to be 40 km s^{-1} at an angle of 55° , and for III 43C was 35 km s^{-1} at an angle of 75° (Indebetouw & Noriega-Crespo 1995). The approximated sizes of the condensations were derived from the position-velocity diagrams in Jijina & Self (1990) and are given in Table 2. The distances between condensations depend on the orientation angle of the slit. For the

1111 43A/43B and 43B/43C pairs their distances are $5.5''/6.9''$, $6.9''/6.9''$ and $6.6''/7.5''$ for 304° , 159° and 146° orientation angles, respectively.

The observed SIDs are wider than the PSF by almost a factor two. The SIDs are so wide that even the 3 condensations models do not match exactly their extent. The models, nevertheless, trace the correct trend of a more extended 'wing' emission from the UV continuum. Something to bear in mind is that the one-dimensional shock models, which are input in the bow shock models, are relatively uncertain at low velocities (~ 20 - 30 km s^{-1}), and furthermore, 1111 1187 did not calculate models at lower velocities than this. For the bow shock models with a peak shock velocities of ~ 35 - 40 km s^{-1} at a relatively large orientation angle, which will have the tendency of enhancing the emission from the 'wings', this is crucial.

The 1111 47A object is one of the four main bowshocks observed in the remarkable 111146-111147 system in the Gum Nebula (see e.g. Wislöffel & Mundt 1994; Burrows, Hester & Morse 1995). It is a low excitation object, with clear spectral features of fluorescent H_2 emission and continuum (Böhm et al. 1991). Given the lack of one dimensional H_2 emission shock models from 1111 1187, we have focused only on the SID of the continuum emission. The model uses a 100 km s^{-1} shock velocity, equilibrium preionization, a preshock density of 100 cm^{-3} , an orientation angle of 23° (into the plane of the sky) and a radius of ~ 3.2 arc seconds (Raga et al. 1987). Observationally the continuum at $1300 - 1900 \text{ \AA}$ (Figure 8) is almost twice as wide as the PSF (Böhm et al. 1991). In this case, however, a single condensation model seems to reproduce the observations, including the 'tail' of the SID. Perhaps the most surprising thing about 1111 47A is that a shock velocity of 100 km s^{-1} works for a low excitation object. A similar conclusion was reached by Curiel et al. (1995) based on their analysis of the GJRS and FOCIST observations, which led them to conclude that a more complex shock structure (C-type magnetic shocks or a MHD precursor) may be present.

5. (conclusions

The goal of this study has been to use a simple kinematical model to understand the spatial intensity distributions observed in the UV light by IUE of some HII objects. The SII models overall have shown that many of the parameters that have been obtained by optical means provide a self-consistent picture when are used to explain the UV emission. The models presented here stress the basic idea that to model the emission of these objects there is the need to include the contribution to the radiation from most of their brighter condensations.

The superposition of two or three bow shocks to mimic the contribution to the UV light seems to match better the observations. This is particularly the case for HII 2(11-A), HII 2(G+B), and 1111 43(A+B+C), which it is not totally surprising given the complexity of these objects. Some of the differences that remain between the observations and the models, we think are in part due to the restrictions imposed on by the preionization of the plane parallel models (e.g. Raymond et al. 1988). This parameter controls the contribution to the emission mainly from low velocity shocks. These shock manifest themselves along the bow shock wings and in this sense control the extent and shape of the SII. This is perhaps the case for the faint and low excitation objects, 111143 and HII 47A, which required low shock velocities to understand their spectra. The uncertainty on their fluxes, the less reliable prediction from the planar shock models in the low velocity range, coupled with their large observed orientation angles, makes the comparison with the models less compelling.

For HII 24A, the single bow shock models (at two different shock velocities), cannot explain simultaneously the different observed SII's. The absence of bright nearby condensations within the IUE aperture prevent us from using the superposition models as to explain its very wide SII. For HII 32A, a single bow shock model with a relatively large viewing angle (between 30°- 70°) and high shock velocity (300 km S-1) reproduces quite well the observed SII.

It is a pleasure to thank Eileen Friel for her support and helpful comments. A.M.-M. was supported by a Perkin Fellowship during her stay at MMO. A.N.-C. research is supported by NASA A Long Term Astrophysics Program through JPL, under contract with Caltech, and NSF grant AST9300391 through MMO.

REFERENCES

- Böhm, K.H., Buhrke, T.H., Raga, A.C., Brugel, E.W., Witt, A. N., & Mundt, R. 1987, ApJ, 316, 349
- Böhm, K.H. 1990, in "Evolution in Astrophysics, IUE Astronomy in the Era of New Space Missions", ESA Conf. proc. sp-31 O, p23
- Böhm, K.H., & Solf, J. 1990, ApJ, 348, 297
- Böhm, K.H., Scott, D. M., & Solf, J. 1991, ApJ, 371, 248
- Böhm, K.H., Noriega-Crespo, A., Solf, J., & Brugel, E.W. 1992, PASP, 104, 251
- Böhm, K.H., & Solf, J. 1992, AJ, 104, 1193
- Böhm, K.H., Noriega-Crespo, A., & Solf, J. 1993, ApJ, 416, 647
- Brugel, E.W. 1989, in "Low Mass Star Formation and Pre-Main Sequence Objects", ed. B. Reipurth, ESO Conference & Workshop Proceedings, No 33, p311
- Brugel, E.W., Böhm, K.H., & Mannery, E. 1981, ApJS, 47, 117
- DeBoer, E. S., & Mcade, M.R. 1981, NASA IUE Newsletter No 15, 53
- Burrows, C., Hester, J., & Morse, J. 1995, HST press release 6/6/95
- Clarke, J.T. & Moos, H.W. 1981 in The Universe at Ultraviolet Wavelengths, ed. R.D. Chapman, NASA cp No 2171, p787
- Curiel, S., Raymond, J. C., Wolfire, M., Hartigan, P., Schwartz, R. D., & Nisenson, P. 1995, ApJ, 453, 322
- Davis, C.J., Eislöffel, J., & Smith, M.D. 1996, ApJ (in press)
- Eislöffel, J., Mundt, R., & Böhm, K.H. 1994, AJ, 108, 1042

- Eislöffel, J., & Mundt, R. 1994, A&A, 284, 530
- Hartigan, P., Mundt, R., & Stocke, J. 1986, AJ, 91, 1357
- Hartigan, P., Raymond, J., & Hartmann, L. 1987, ApJ, 316, 323
- Hartigan, P., 1989, ApJ, 339, 987
- Hartmann L., & Raymond, J. 1984, ApJ, 276, 560
- Herbig, G., & Jones, B.F. 1983, AJ, 88, 1040
- Hester, J. J., Scowen, P. A., Lynds, R., & O'Neil, E.J. 1994, BAAS, 26, 1386.
- Indebetouw, R., & Noriega-Crespo, A. 1995, AJ, 109, 752
- Jones, B.F, Cohen, M., Wehinger, P. A., & Gehren, T. 1987, AJ, 94, 1260
- Lee, M. G., Böhm, I{.11., Temple, S.1.), Raga, A.C., Mateo, M.L., Brugel, E.W., & Mundt, R.
1988 AJ, 96, 1690
- Noriega-Crespo, A., Böhm, I{.11., & Raga, A.C. 1989, AJ, 98, 1388
- Mundt, R., Ray, T.P., & Raga, A.C. 1991, A&A, 252, 740
- Raga, A.C. 1989, AJ, 98, 976
- Raga, A.C., & Noriega-Crespo, A. 1993, RMxAA, 25, 149
- Raymond, J.C, Hartigan, P., & Hartmann, L. 1988, ApJ, 326, 323
- Reipurth, H., Heathcote, S., Roth, M., Noriega-Crespo, A., & Raga, A.C. 1993, ApJ, L49
- Schwartz, R.D. 1975 ApJ, 195, 631
- Schwartz, R.D. 1978 ApJ, 223, 884
- Schwartz, R.D., Cohen, M., Jones, B.F., Böhm, I{.11., Raymond, J.C., Hartmann, L. W.,
Mundt, R., Dopita, M. & Schultz, A.S.B. 1993, AJ, 106, 740

Solf, J., Böhm K.H., & Raga, A.C. 1986, ApJ, 305, 795

Solf, J. 1987, A&A, 184, 322

Turnrose, B. E., & Thompson, R. W. 1984, 1 U}! Processing Manual (Computer Science Corporation, Beltsville, MD.)

Figure Captions

Figure 1. Bow shock geometry. The gas enters the bow shock at a velocity V_S and angle ξ . The parallel component of the velocity ($V_{parallel}$) is conserved across the shock, perpendicular component is thermalized (from $V_{perp,i}$ to $V_{perp,f}$). The angle between the plane of the sky and the symmetry axis of the bow shock is ϕ .

Figure 2. A sample of the spatial intensity distributions (SID) created by the kinematical bow shock model for the high excitation C IV $\lambda 1549$ and the low excitation Mg II $\lambda 2799$ emission lines (top panels). The models correspond to a set of shock velocities of 100, 150, 200, 250 km S^{-1} , at two different initial gas preionizations: equilibrium (eq) and full (fp). A sample of the plane parallel models used to obtain the SID is shown at the bottom panel, which corresponds to the intensity radiated by the shock as a function of the shock velocity for the C IV $\lambda 1549$ (eq) and Mg II $\lambda 2799$ (fp) lines.

Figure 3. Comparison of the observed and theoretical spatial intensity distribution of HII 1, for the C IV $\lambda 1549$ and the Si III] $\lambda 1891$ lines, and two continuum bands 200 \AA wide. The IUE point spread function (broken line) and the convolution of the model with it (solid line) are plotted.

Figure 4. As in Figure 3, but for the HII 2(H+ λ) condensations in the C IV $\lambda 1549$ and C III] $\lambda 1909$ lines for two different IUE observations SWP40663 (top) and SWP18157 (center) (see Table 1) using the superposition of two bow shock models. The distributions for the same lines but for the HII 2(G+B) condensations (bottom)

Figure 5. As in Figure 3, but for the continuum distributions at 1300 – 1500 \AA and 1600

1800 Å for 1111 24A. The observations correspond at two different aperture orientations. The SWP22708 (top) and SWP38033/102 (center) distributions are compared with a model with a shock velocity of 50 km s^{-1} . The SWP38033/102 set (bottom) is also compared with a model at a 100 km s^{-1} shock velocity.

Figure 6. As in figure 3, but for the Mg II $\lambda 2799$ line in III 32A. Two models with different viewing angles are compared: 300° (top) and 70° (bottom), with the same 300 km s^{-1} shock velocity.

Figure 7. As in Figure 3, but for the III 43(A+B+C) system and a triple condensation model and three different continuum observations: 200, 400 and 600 Å wide, respectively.

Figure 8. As in Figure 3, but for the 600 Å wide continuum distribution of III 47A.

Table 1. Archival IUE Spectral Data

Name object	Image no.	Exposure time(min)	Orientation angle(deg)	Roll angle(deg)	Years of observation
11111	SWJ' 8188	270	337	95.9	1980
	SWP16668	270	348	84.6	1982
	SWP24914	729	303	130.5	1985
	SWP40657	633	315	124.7	1991
	LWR 8912	134	167	266.1	1980
11112(11-IA')	SWP10218	270	165	268.4	1980
	SWP10246	290	167	266.3	1980
	SWP16671	430	349	84.0	1982
	SWP18157	430	167	266.1	1982
	SWP24919	860	304	129.4	1985
	SWP40663	675	312	123.8	1991
	LWR 8888	180	165	268.4	1980
	LWR 8909	150	167	266.4	1980
	LWR10450	380	5	67.8	1981
III 2G	SWP43891	636	315	119.0	1992
III 24A	SWP21518	560	189	243.9	1983
	SWP22708	485	153	81.3	1984
	SW P38033	680	307	126.3	1990
	SWT38102	585	320	113.3	1990
	LWP 3140	120	153	81.3	1984
III 32A	LWR13004	414	155	-99.0	1982
111143	SWP17522	390	132	301.1	1982
	SWP23749	425	147	285.7	1984

Table 1- Continued

Name object	Image no.	Exposure time(min)	Orientation angle(deg)	Roll angle(deg)	Year of observation
III 47A	SWP24924	580	304	128.7	1985
	SWP31828	781	159	275.3	1987
	LWP 4041	420	146	286.8	1984
	SWP17549	400	78	355.4	1982
	SWP21389	440	168	264.6	1983
	SWP32154	411	128	-99.0	1987
	SWP33960	870	340	4.2	1988

Table 2. Best Fit Bow Shock Model Parameters¹

Object	V_{sh} (km S ⁻¹)	$\phi(^{\circ})$	Radius('')
HH 1	175	5	2.0
HH 2A'	170	12	1.7 ²
			1.83
			2.84
HH 2}1	125	2	2.5 ²
			2.4 ³
			1.54
HH 2G	110	-5	0.9
HH 2B	105	2	0.4
HH 24A	50	-36	3.0
	100	-36	3.0
HH 43A	100	60	2.3
HH 43B	40	55	2.5
HH 32A	300	30	2.5 ⁵
	300	70	2.5 ⁵
HH 43C	35	75	1.8
HH 47A	100	23	3.2

¹Most models are in equilibrium preionization²Orientation angle = 5°³Orientation angle = 1 65°, 349°⁴Orientation angle = 304°, 312°⁵Fully preionized

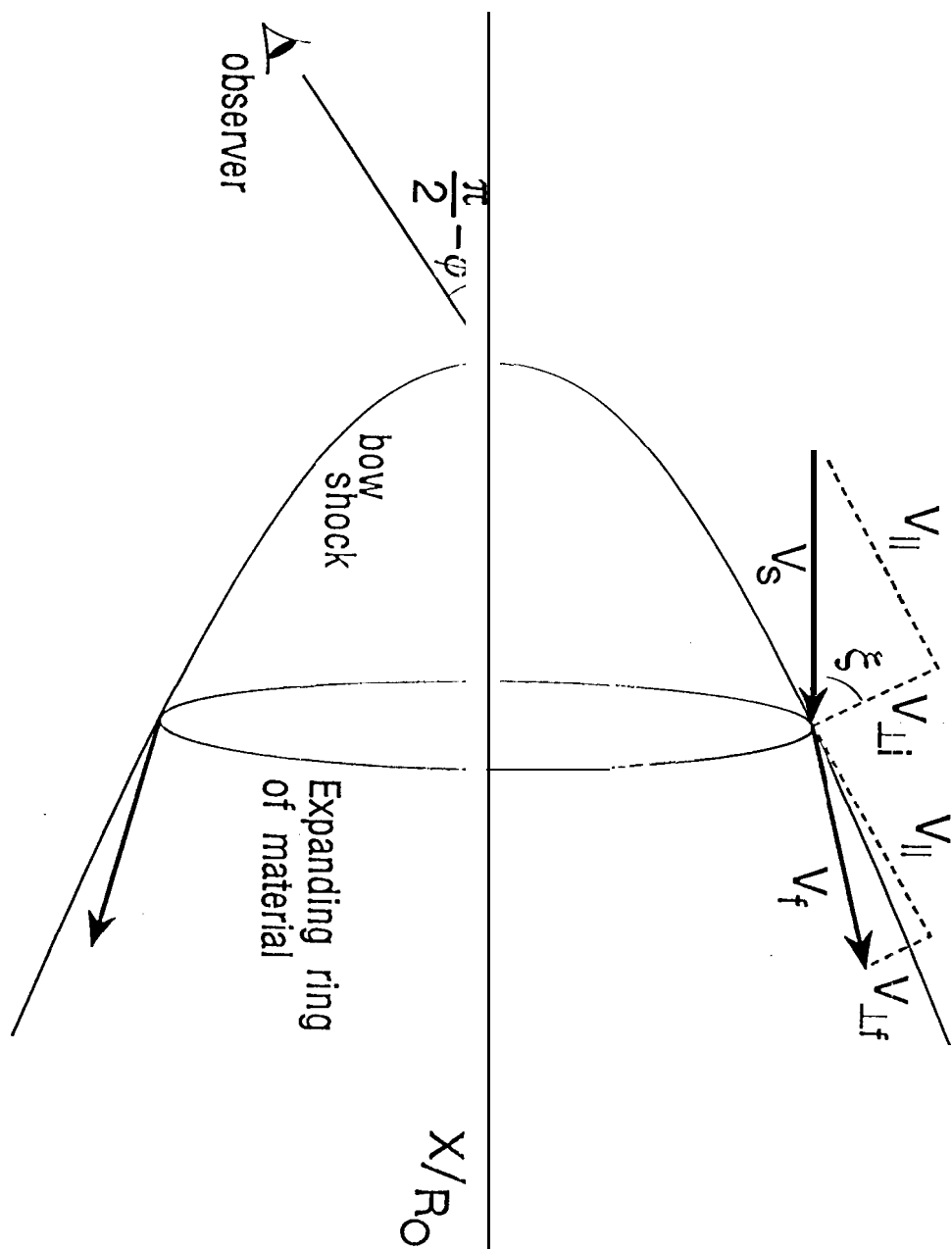


Fig 1
Moro-Morlin et al. 1996

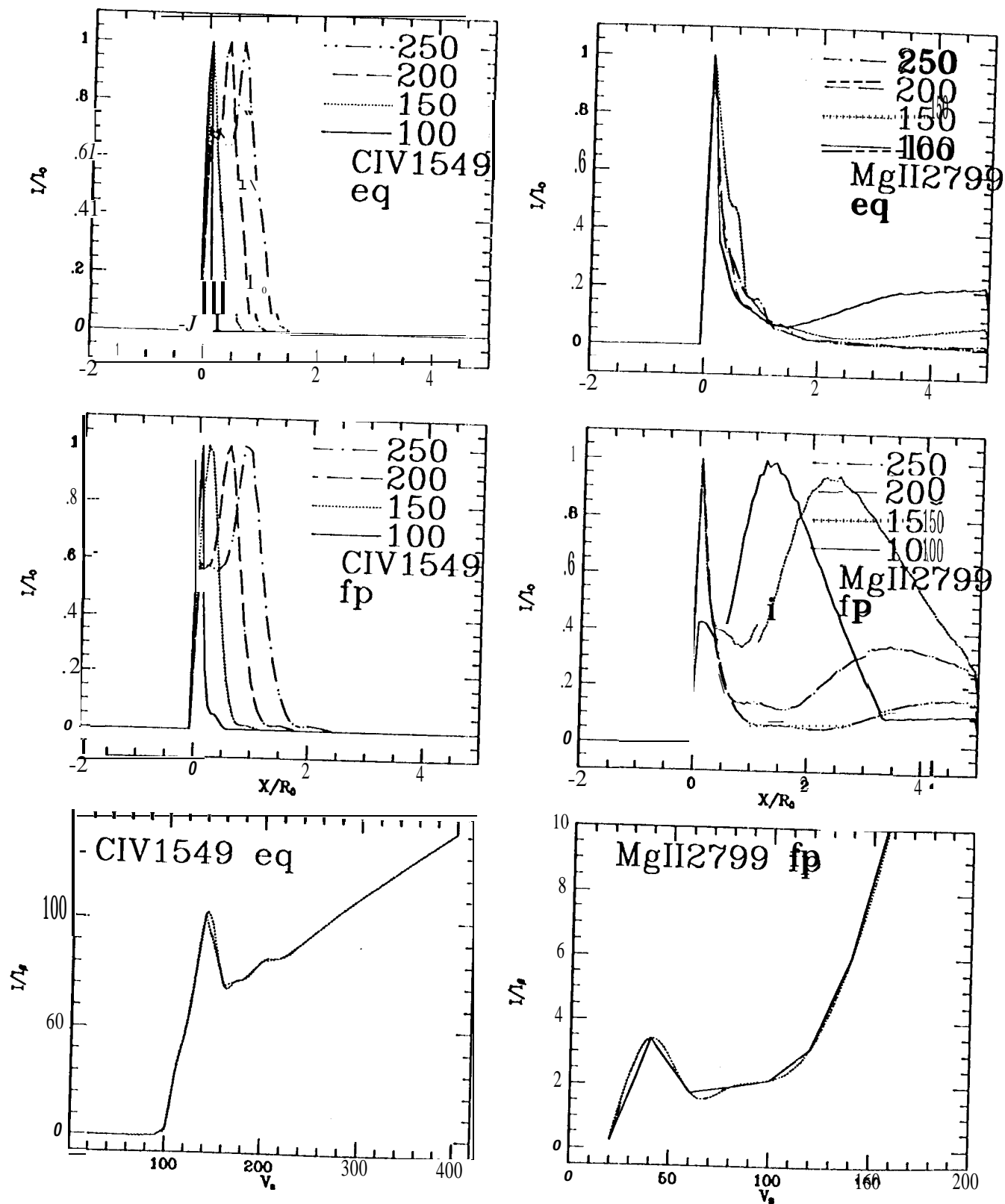


Fig 2.
Moro-Martin et al 1986

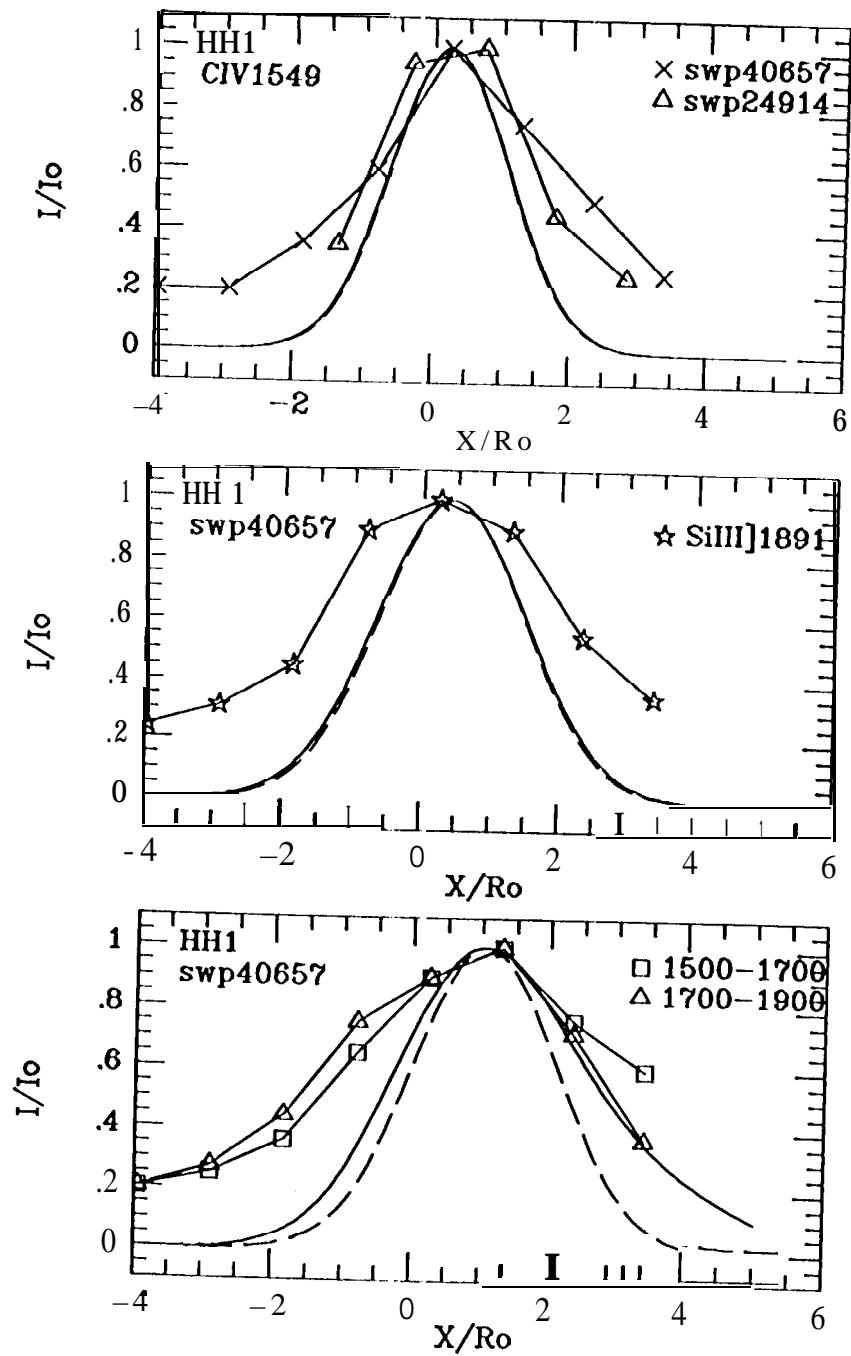


Fig 3.
Moro-Martin et al. 1996

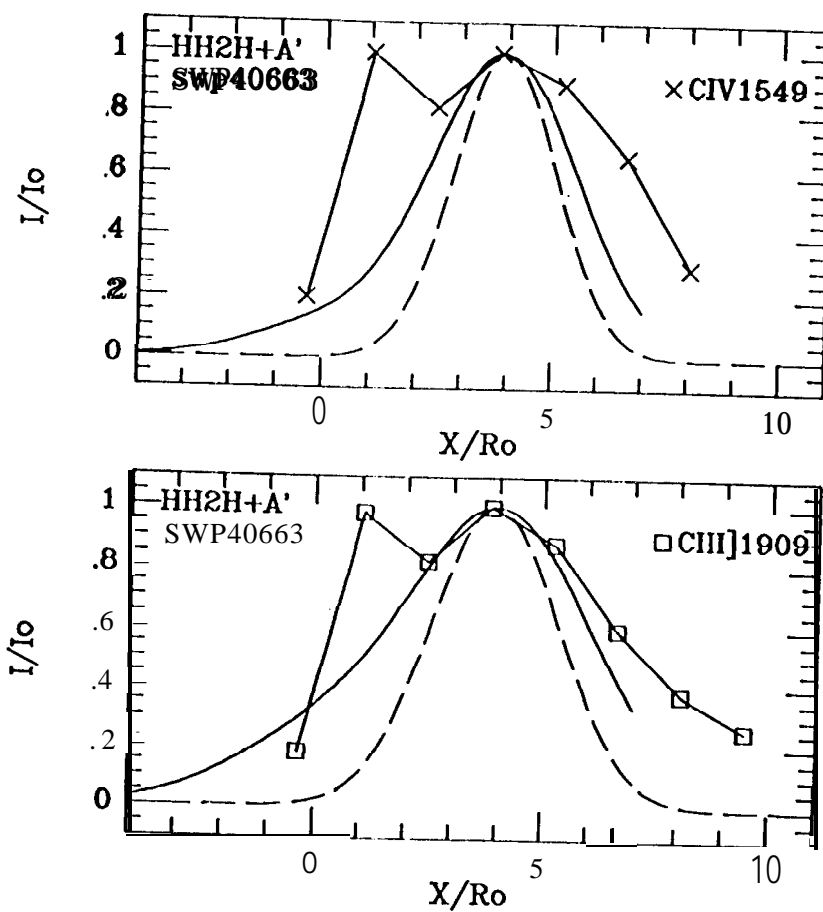


Figure 4a
Moro-Martín et al. 1996

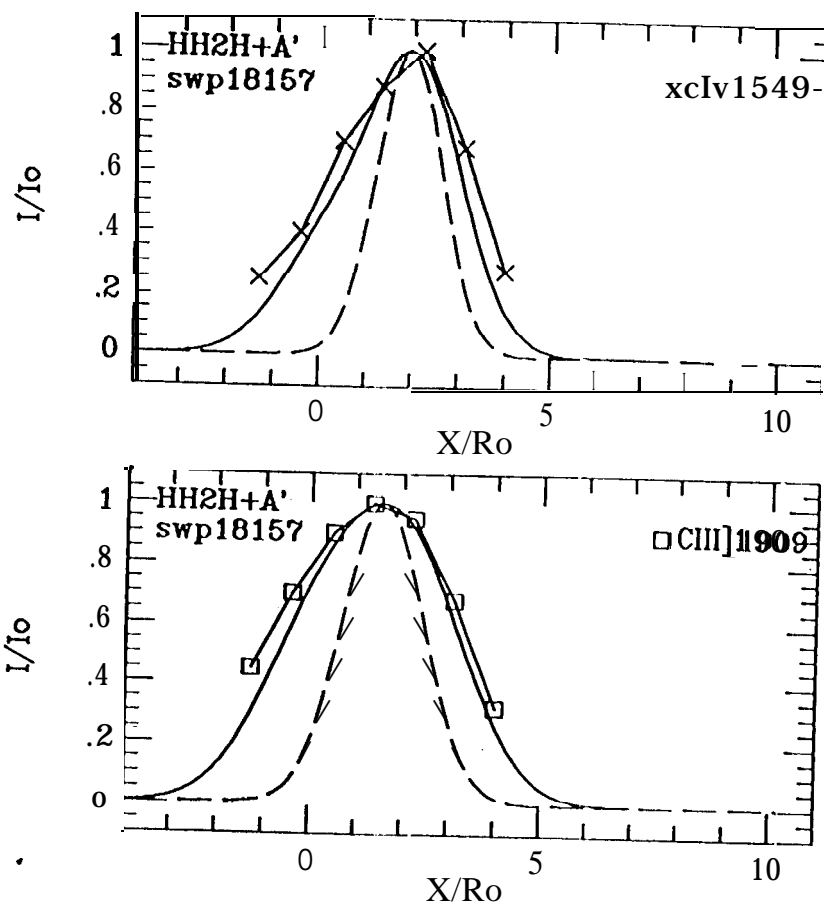


Figure 4b
Moro-Martin et al. 1996

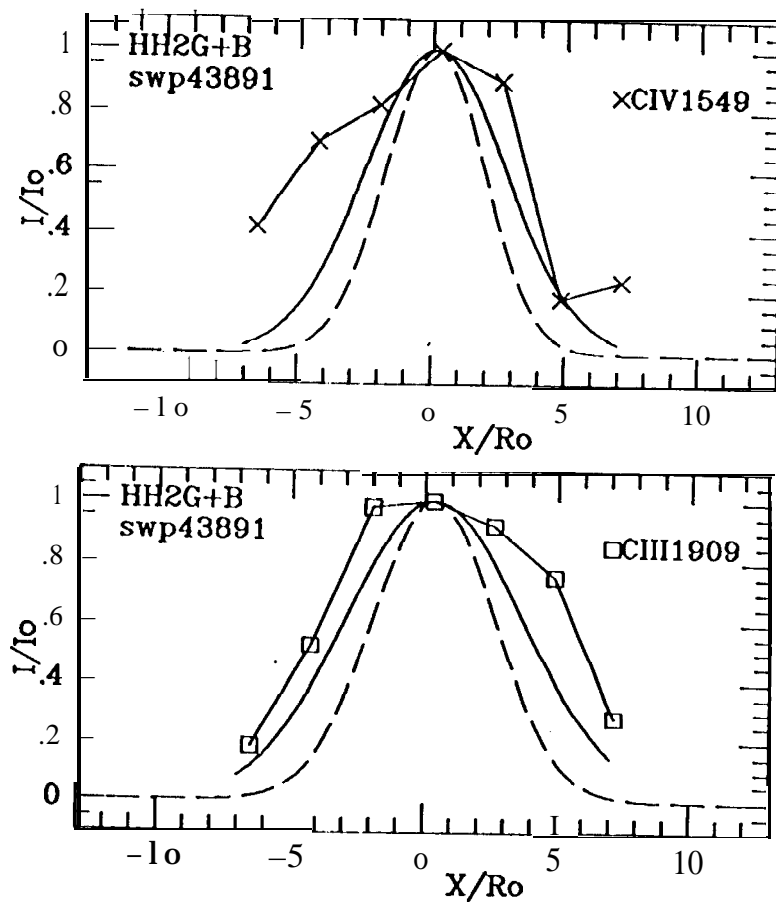


Figure 4c
Mow-Martin et al.

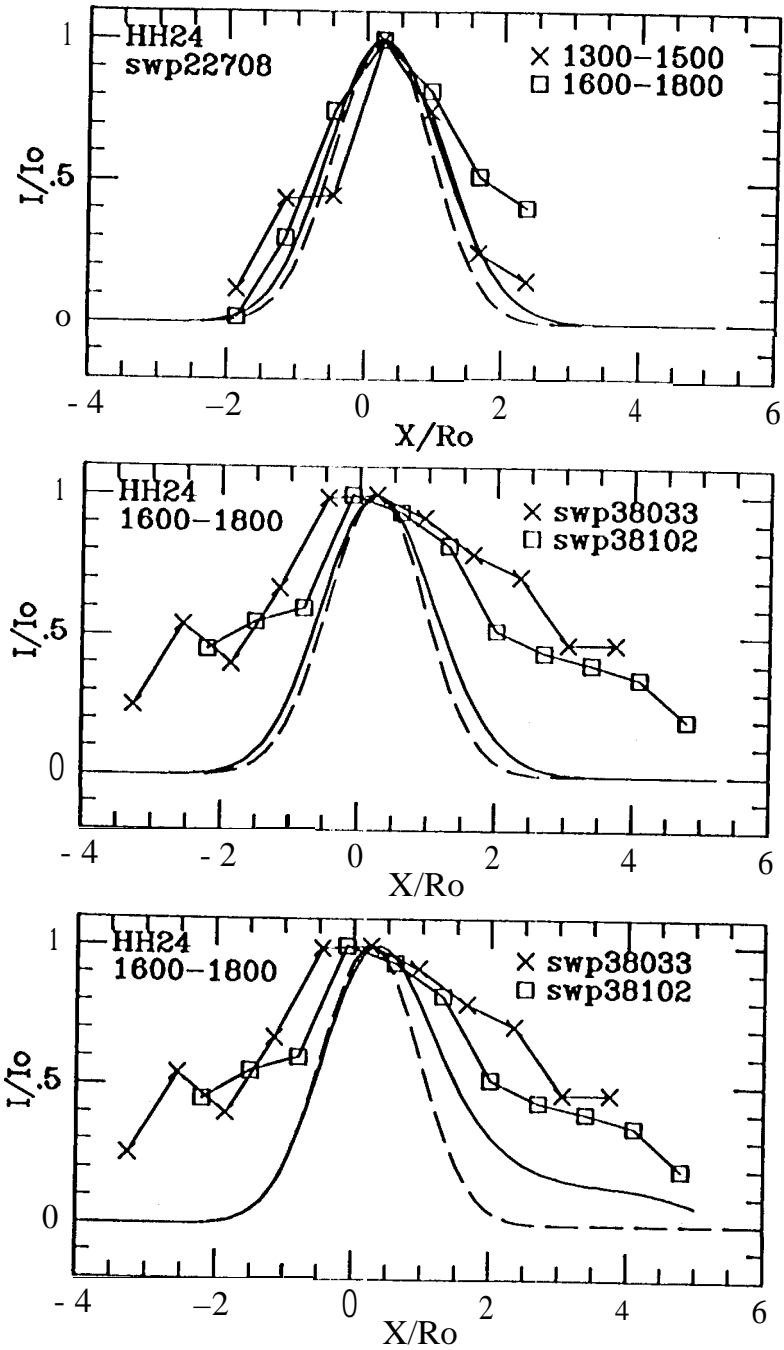


Figure 5
Moo-Martin et al. 1996

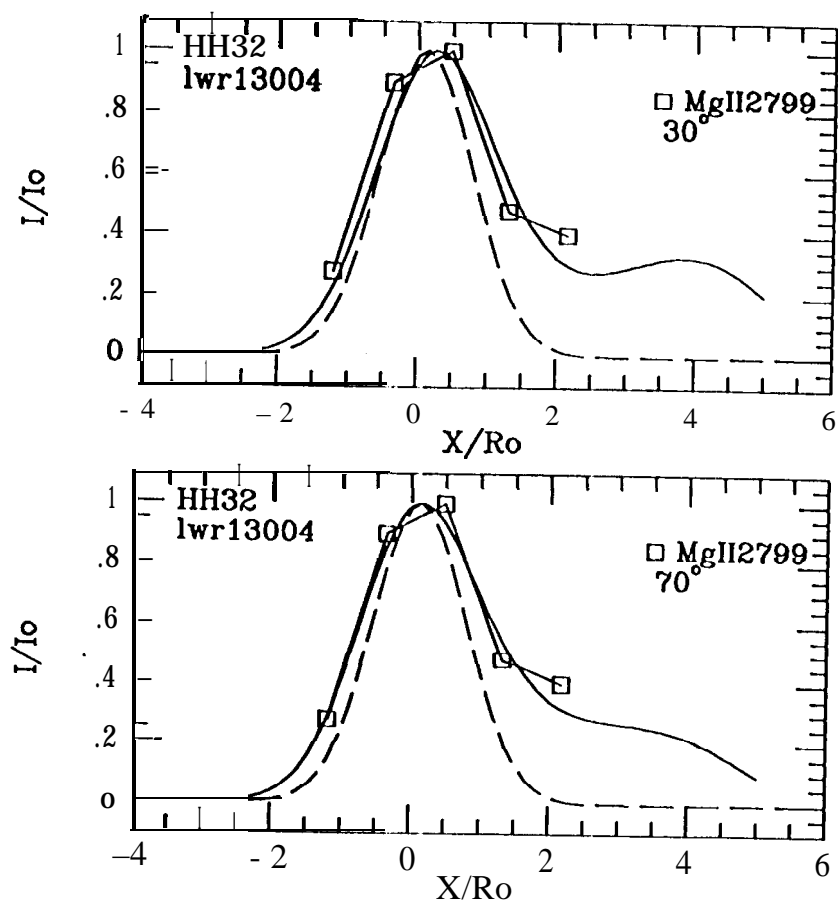


Figure 6
Moro-Martin et al. 1996

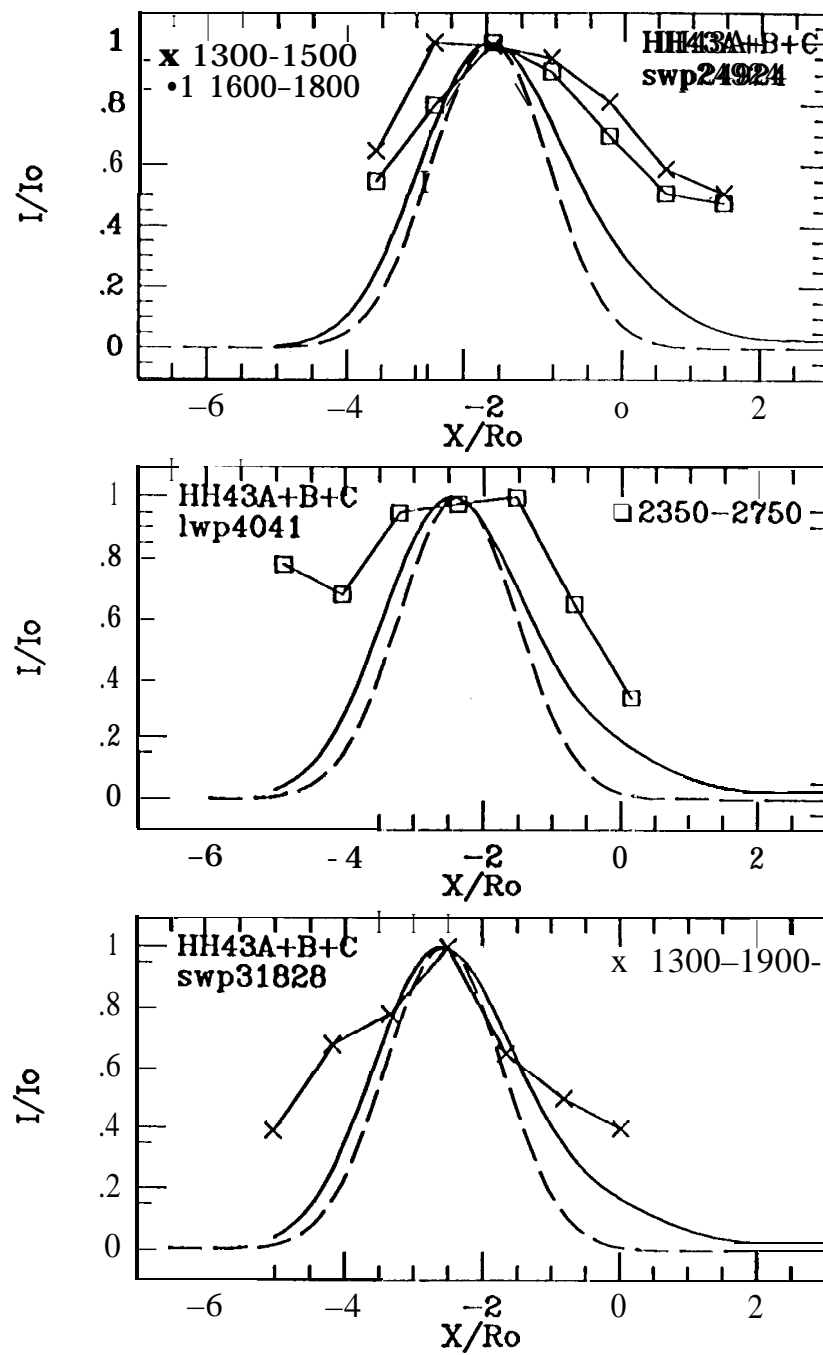


Figure 7
Moro-Martinez et al., 19

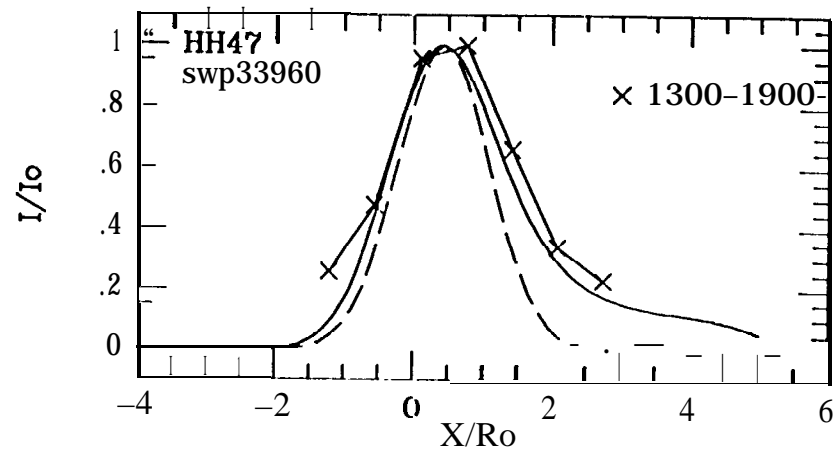


Figure 8
Moro-Martin et al. 1981